Title

Surface Energy Measurements of Yttrium Oxide

Author

Joshi, Kavan Sajaykumar

Publication Date

2023

Peer reviewed|Thesis/dissertation

Surface Energy Measurements of Yttrium Oxide

By

KAVAN JOSHI

THESIS

Submitted in partial fulfillment of the requirements for the degree of MASTER OF SCIENCE

in

MATERIALS SCIENCE AND ENGINEERING

in the

OFFICE OF GRADUATE STUDIES

of the

UNIVERSITY OF CALIFORNIA

DAVIS

Approved by:

Ricardo H. R. Castro, Chair

Jeremy Mason

Scott J McCormack

Committee in Charge

2023

Table of Content

Acknowledgments iii

Abstract iv

Chapter 1: Introduction 1

1.1 Motivation 1

1.2 *Hypothesis* 2

1.3 *Objective* 2

Chapter 2: Synthesis of yttria nanostructures and surface energy analysis 3

2.1 Introduction 3

2.1.1 Thermodynamics of Sintering 4

2.2 Experimental Methods 5

2.2.1 Synthesis of nanostructure 5

2.2.2 Materials Characterization 8

2.2.3 BET 9

2.2.4 Water Adsorption Calorimetry 11

2.3 Results and Discussion 15

Chapter 3: Atomistic Simulations for Surface Energy Measurement of Y_2O_3 23

3.1 Introduction 23

3.2 Methods and molecular dynamics setup 24

3.2.1 Verification of various interactions models: 25

3.2 Results 28

Chapter 4: Correlation and Prediction of Surface Energies of Y_2O_3 **34**

4.1 Discussion 34

Chapter 5: Conclusion and Future works **37**

5.1 Conclusion 37

5.2 Future work 37

Reference **49**

Acknowledgment

I would like to express my heartfelt gratitude to everyone who has been a part of my journey in completing my master's thesis at UC Davis.

First and foremost, I would like to thank my beloved family, my father, Dr. Sanjay Joshi, my mother, Payal Joshi, and my brother, Kathan Joshi, for their unending love, encouragement, and unwavering belief in my abilities. Their constant support has been a source of strength, motivating me to persevere and achieve my academic goals.

I am deeply indebted to my advisors, Prof. Ricardo Castro, and Prof. Jeremy Mason, for their exceptional guidance, support, and advice throughout my research endeavor. Their unwavering patience during my learning process and progress was truly remarkable. I am truly privileged to have had the opportunity to work under their guidance.

I would also like to thank my lab mates, Isabella, Raven, Luis, Victor, Spencer, and Connor, for taking their time and helping me with various characterization techniques. The discussions and valuable feedback have been integral to my growth as a researcher and have enriched my academic experience. Above all, I extend my sincerest appreciation to Nicki, whose unwavering support and friendship have been invaluable during my time at Davis. Her kindness and encouragement have made a significant difference in my journey, and I am grateful for having such an amazing friend.

I am grateful to the faculty members and staff of the Materials Science and Engineering at UC Davis for their dedication to academic excellence and fostering a nurturing learning

environment. Their passion for teaching and commitment to research have been instrumental in shaping my academic journey.

I extend my thanks to National Science Foundation for providing the financial support that enabled me to conduct my research and realize my academic aspirations.

To all the researchers and authors whose works have contributed to the foundation of my research, I express my appreciation for their groundbreaking studies and discoveries that have enriched the context of my thesis.

Last but not least, I want to acknowledge my friends and colleagues for their encouragement and camaraderie. Your support has been a constant source of inspiration and motivation.

In conclusion, the completion of this Master's thesis has been an incredible learning experience, and I am truly grateful to each and every person who has contributed to its successful completion.

Abstract

Nanoceramics have unique properties compared to bulk materials, primarily because of their large interfacial areas. This gives rise to considerable surface and grain boundary energies that play an important role in thermodynamic stability and the sintering process. During sintering, densification of the nanoceramic occurs by the mass transport phenomena, and the reduction of interfacial energy is the driving force for this process. Experimental thermodynamic data on surface energies, and in particular on free surface energies, is lacking, though. Yttrium oxide is selected as a model material because of its wide range of applications and abundant sintering studies in the literature. Faceted nanocrystalline yttrium oxide was synthesized by hydrothermal synthesis, and the morphology of these nanoceramics was studied using electron microscopy. Surface energies of specific planes were determined experimentally by water adsorption calorimetry using an experimental setup that includes a water micro-dosimeter combined with a micro-calorimeter. This characterization technique is based on the thermodynamics of water adsorption on the anhydrous surface of the ceramics. Molecular dynamic simulations were also performed to estimate the free surface energies as a function of the surface normal, and corroborate the experimental results.

Chapter 1: Introduction

1.1 Motivation

Sintering, one of the oldest human processing techniques, originated in the prehistoric era with pottery firing. However, the fundamental and scientific study of sintering started in the 1940s. Following that, sintering has become an essential and well-studied processing technique that produces dense ceramics. In the modern era, the most beneficial and vital application of sintering is the fabrication of various kinds of sintered parts, from bulk ceramic components to powder metallurgical parts.

Sintering is identified as a complicated microstructure evolution involving various mass transport mechanisms. The driving force in the sintering process is the elimination of excess surface energy. While there has been considerable study of the effects and implications of this for the sintering of traditional ceramic powders, the situation is different with the sintering of nanoparticles, where the significantly increased surface area and surface energy changes the sintering process. The sparse experimental literature on the sintering and densification of nanoparticles is also a limiting factor in deducing whether current sintering theories are inadequate or if there are experimental complications such as contamination or aggregation.

Furthermore, there is minimal experimental thermodynamic data on surface energies for specific surface orientations which are essential for accurate simulations of ceramic processing. Tam recently stated [1] "There are no experimental data on the surface[s] of differently oriented rare earth oxide surfaces", and this holds for other oxides as well. This presents a substantial

opportunity to measure the energies of individual surfaces of rare earth oxides and to use this to support the eventual fabrication of parts by the sintering of nanoparticles [2-4].

1.2 Hypothesis

We hypothesize that the experimental and theoretical thermodynamic data of the surface energies of ceramic oxides at different crystallographic orientations will eventually enable us to accurately predict microstructural evolution and grain growth during the sintering process.

1.3 Objectives

The objectives of this research were to explore the different surface energies of yttrium oxide through the following careful experimental and computational techniques:

1 Synthesize nanostructures of Y_2O_3 with different surface facets using reverse strike co-precipitation and hydrothermal synthesis.

2 Evaluate the morphology of the nanostructures using electron microscopy.

3 Determine the surface energies of the nanostructures by water absorption experiments.

4 Perform atomistic simulations to corroborate the inferred surface energies.

Chapter 2: Synthesis of yttria nanostructures and surface energy analysis

2.1 Introduction

Yttrium oxide (Y_2O_3) was chosen as a model material to study the sintering process as there is extensive literature on the sintering of yttria using techniques such as spark plasma sintering, flash sintering, and two-step sintering. Furthermore, yttria does not show significant structural and chemical changes over a wide range of working temperatures. Due to this fact, Y_2O_3 serves as a functional material for a variety of applications, especially when sintered, and enables the fabrication of transparent ceramics with optical applications such as laser hosts and scintillators [5-8].

Recent developments have demonstrated the possibility of directly measuring the surface energies of ceramic particles using microcalorimetric techniques [9, 10]. This methodology inherently provides surface energy data averaged over all surface planes of the particle, weighted by their respective surface areas. Although this average surface energy data is valuable for enhancing our understanding of sintering, knowing the surface energy values of specific crystallographic planes would enable more precise theoretical calculations of microstructural evolution. Additionally, it would provide fundamental information about anisotropic phenomena that can occur during the sintering process.

2.1.1 Thermodynamics of Sintering

The driving force for sintering is the excess energy deriving from surfaces and grain boundaries, and the change in these free energies during the sintering process is described as

$$\Delta G = \gamma_s \Delta A_s + \gamma_{GB} \Delta A_{GB} \quad (1)$$

where G is the total interfacial energy of the system, γ_s and γ_{GB} are the surface and grain boundary energies, respectively, and A_s and A_{GB} are the surface and grain boundary areas of the system. Moreover, Lange et al. [11-14] showed that the thermodynamic favorability of densification during the initial stages of sintering, which is comprised of neck formation and pore shrinkage, is determined by the ratio of grain boundary energy and surface energy. This ratio is described through Young's relation as

$$\frac{\gamma_{GB}}{\gamma_S} = 2cos\left(\frac{\phi_e}{2}\right) \quad (2)$$

where ϕ_e is the equilibrium dihedral angle between particles at the neck that forms during the early stages of sintering. The instantaneous contact angle (ϕ) reaches equilibrium when the free energy change attains a local minimum, and the initial densification stops. Further densification can happen only when mass is transferred from one particle to another during the intermediate and final stages of sintering (the coarsening phase). Hence, the higher the equilibrium dihedral angle and the lower the grain boundary to surface energy ratio, the higher the densification in the initial stages of the sintering process. Wakai et al. [15] directly modeled this using a three-particle array.

However, there is a significant assumption that the surface and grain boundary energies are isotropic. Considering the crystallographic nature of the particles in the ceramic structure, there could be substantially different surface and grain boundary energies for different surface or boundary plane directions. Yttria being a cubic crystal with a $I\bar{a}3$ space group, it is expected that the {111} type plane should have the least surface energy. This would lead to dihedral angles in the microstructure that depend on the orientation of the adjoining crystals, increasing the complexity of the interfacial thermodynamics during sintering. Searcy et al. [16] have theoretically predicted the effects of surface energy anisotropy on the driving force of sintering, though the experimental difficulty in measuring surface energies for each surface plane has been a challenge.

2.2 Experimental Methods

2.2.1 Nanostructure synthesis

Three morphologically different nano-crystalline structures were synthesized for this study.

Y_2O_3 nanoparticles were synthesized using the standard method of Nakajima et al. [5] that uses reverse-strike co-precipitation. Figure 1 shows a schematic of the process. Yttrium nitrate hexahydrate ($Y(NO_3)_3.6H_2O$, 99.9 %, Alfa Aesar) was the metal precursor. A 1 mol/L solution was produced by dissolving the yttrium nitrate into deionized (DI) water. This acidic solution was then dripped slowly into a basic solution of ammonium hydroxide at a concentration of 5 mol/L and was vigorously stirred on a stir plate with no heat. Supersaturated conditions were prepared in the basic solution using five times the amount of ammonium hydroxide necessary to

complete the reaction with yttrium nitrate. These conditions assured the fast completion of the reaction in the solution and controlled the pH fluctuations that occurred during the reaction to ensure a uniform size distribution of the particles. The reaction of the nitrate with the hydroxide formed yttrium hydroxide precipitates. These precipitates were separated from the solution by centrifuging the suspension at 3000 rpm for 5 minutes. The hydroxide precipitates were washed in a centrifuge with anhydrous ethanol and DI water three times each. A drying oven was used to dry the precipitate for two days at 80 ^{o}C. Nanoparticles were obtained after grinding the powder using a mortar and pestle and then calcining it at 700 ^{o}C for 3 hours in a box furnace (Thermo Scientific Lindberg Blue M).

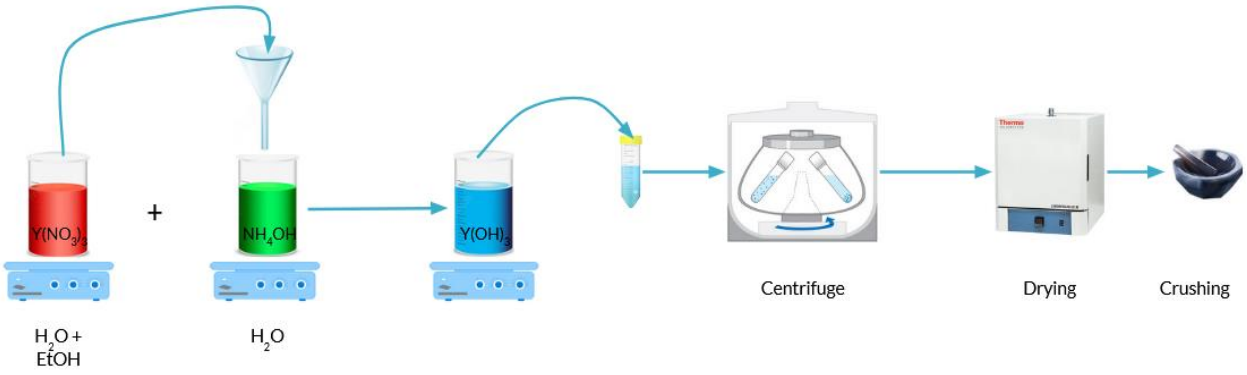

Figure 1: Schematic representation of the reverse-strike co-precipitation method for yttrium oxide nanoparticle synthesis.

The synthesis of two different highly oriented nanostructures was done using the hydrothermal synthesis method. Figure 2 shows a schematic of the synthesis process. The first nanostructure was pure Y_2O_3 nanosheets, synthesized using the method of Matsunaga et al. [17] as a reference. The metal precursor was yttrium nitrate hexahydrate ($Y(NO_3)_3.6H_2O$ 99.9 %, Alfa Aesar). Yttrium nitrate was first dissolved in deionized water, making a solution with a total volume of

20 ml. The amount of yttrium nitrate was set based on the desired amount of Y_2O_3. Ethylene glycol (anhydrous, 99.8 %, Sigma-Aldrich) was added to this solution to make the moles of ethylene glycol five times that of yttrium nitrate. The solution was stirred for 10 minutes, and then triethylamine (≥ 99 %, N, N-Diethylethanamine, TEA, Sigma-Aldrich) was added such that the number of moles was twice that of yttrium nitrate. The excess triethylamine and ethylene glycol ensured that the reaction was almost complete. DI water was added to bring the total volume of the solution to 40 ml, and the resulting solution was stirred for 10 min. The solution was then transferred to a Teflon vessel with a volume of 100 ml and was heated inside an autoclave (Parr Instrument Company) at 160 ^oC for 24 hours. After 24 hours it was cooled down to room temperature, and the solution was centrifuged at 3000 rpm for 5 minutes to separate the precipitate. This was followed by washing with DI water and ethanol three times each. The precipitate was dried in an oven at 80 ^oC for 5 hours to obtain the precursor. The precursor was crushed to get a powder using a mortar and pestle and calcined at 600 ^oC for 2 hours in a box furnace (Thermo Scientific Lindberg Blue M) to obtain the Y_2O_3 nanosheets.

For the nanorods, the same precursor was used as in the previous synthesis methods, i.e., yttrium nitrate hexahydrate ($Y(NO_3)_3.6H_2O$ 99.9 %, Alfa Aesar). The hydroxide agent used was sodium hydroxide pellets (NaOH, fisher chemical). The method suggested by Priya et al. [18] was used to synthesize nanorods of Y_2O_3. At first, the yttrium nitrate weighed according to the desired mass of yttrium oxide was dissolved in DI water to get a total volume of 20 ml. Then a 2 M solution of NaOH was added to the nitrate solution dropwise until the number of moles of NaOH was 15 times that of yttrium nitrate. The pH of the solution was monitored with the help of a pH meter (FiveGo, Mettler Toledo) and maintained at 13. Precipitates formed as the hydroxide

solution was added, and the solution was continuously stirred using a magnetic stirrer until 30 min after the addition of the hydroxide. This solution was then added to a Teflon vessel (Parr Instrument Company) and placed inside an autoclave for hydrothermal synthesis. The autoclave was heated to 180 ^{o}C for 24 hours in a furnace. After cooling the autoclave to room temperature, the solution was taken from the Teflon vessel and centrifuged at 3000 rpm for 5 minutes to isolate the precipitate. Then the precipitate was centrifuged and washed using ethanol and water three times each. The precipitate was dried in an oven at 80 ^{o}C for 6 hours and crushed using a mortar and pestle to form a powder. Finally, the powder was calcined at 500 ^{o}C for 2 hours to get Y_2O_3 nanorod powder in a box furnace (Thermo Scientific Lindberg Blue M).

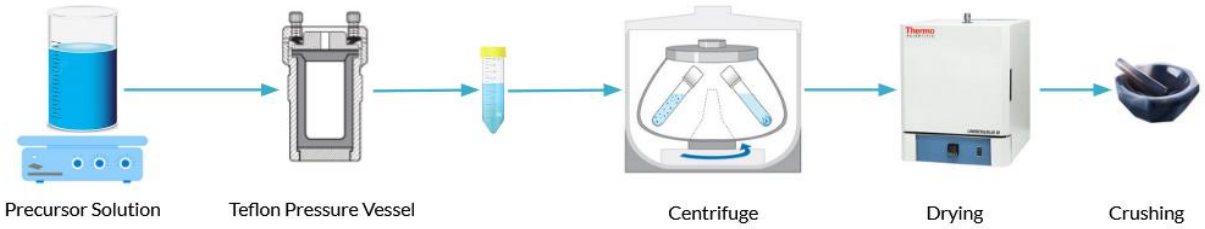

Figure 2: Schematic representation of the hydrothermal synthesis for yttrium oxide nanosheets and nanorods.

2.2.2 Materials Characterization

The crystallographic phases of the synthesized nanoparticles, nanosheets, and nanorods were determined using X-ray diffraction (XRD, Bruker AXS Inc. Madison, WI, USA) with a scan range of 15^{o} to 90^{o} and Cu K-alpha radiation (λ = 1.5406 Å, 40 kV, 40 mA). The surface area of each sample was analyzed by the Brunauer-Emmer-Teller (BET) method through nitrogen adsorption with a Gemini VII Surface Area Analyzer (Micromeritics Instruments Corp.,

Norcross, GA, USA). The morphology of the particles was studied by scanning electron microscopy with an FEI Nova Nano SEM 430 (CNM2, UC Davis) and transmission electron microscopy with a Joel JEM2100 (I-FMD, Lehigh University). The surface energies of the nanostructures were measured by water adsorption microcalorimetric experiments which used a 3Flex surface characterization (Micromeritics Instruments Corp., Norcross, GA, USA) coupled with a Calvet type microcalorimeter Sensys Evo DSC (Setaram, KEP Technologies, Caluire, France).

2.2.3 BET

The BET theory works on the principles of gas adsorption on the materials' surface. This is caused by the van der Waals forces exerted between the adsorbate and the surface. The amount of the adsorbed gas is correlated with the surface area of the adsorbent material and depends on various other factors including the exposed surface, temperature, gas pressure, and strength of the interaction between the adsorbent material and the adsorbed gas. The BET theory extends the concepts of the Langmuir theory [19]. The Langmuir theory considers the ideal situation where there is a relationship between the adsorption of gas molecules forming a monolayer on a solid surface and the gas pressure of the surrounding medium at a constant temperature. However, the BET theory observes multilayer adsorption isotherms that address some shortcomings of the Langmuir theory. The BET theory assumes that all the multilayers are in equilibrium without any interactions between the layers, allowing the Langmuir equation to be applied to each layer. The molecules in the layers below the initial layer serve as the adsorption sites for the molecules in the layer above. The BET equation is expressed as:

$$\frac{1}{X[(P_o/P)-1]} = \frac{1}{X_m C} + \frac{C-1}{X_m C}\left(\frac{P}{P_o}\right) \quad (3)$$

where X is the weight of the adsorbed gas at a relative pressure (P/P_o), X_m is the monolayer capacity of the adsorbed gas which is the volume of the gas adsorbed at standard temperature and pressure, and C is a constant [19].

Nitrogen gas was the adsorbed gas as it strongly interacted with the solids. Since the interactions between the solid and the gas phase are weaker, the sample was cooled using a liquid nitrogen bath to achieve a measurable amount of adsorption. A fixed amount of nitrogen is released at each step onto the sample. After reaching the saturation pressure there is no additional adsorption even if more gas is added. Highly accurate and precise pressure transducers monitor the pressure change. The data collected is represented as a BET isotherm which shows the amount of adsorbed gas as a function of the relative pressure.

Ideally, five data points would be sampled in the interval 0.025 to 0.3 of relative pressure to determine the surface area using the BET equation. There is the onset of capillary condensation at relatively high pressures, and at relatively low pressures only monolayer formation has occurred. The least squares regression method calculates the plot's slope (indicated by the variable *s*) and intercept (indicated by the variable *i*). The following equation determines the monolayer capacity:

$$X_m = \frac{1}{s+i} \quad (4)$$

The total surface area can then be determined by the following equation using the value of X_m:

$$S = \frac{X_m L_{av} A_m}{M_v} \quad (5)$$

where L_{av} is Avogadro's number, A_m is the cross-sectional area of the adsorbate and equals 0.162 nm^2 for a nitrogen molecule, and M_v is the molar volume of 22414 ml [20, 21].

2.2.4 Water Adsorption Calorimetry

Several methods are available to measure the surface energies of materials. Some standard techniques are to measure wetting angle [22], correlate surface energies to elastic modulus [23], and to use a calorimetric approach. Two calorimetric methods have been used more extensively in the past decade to measure surface energies of oxides: high-temperature oxide melt solution [24-26] and water adsorption calorimetry [9]. The prior one has some limitations in that the samples used to measure the heat signals should have different surface areas but similar shapes and similar exposed crystallographic planes. This is because the heat of the drop solution depends linearly on the surface areas, and to infer the surface energies all other contributions to the heat need to be known or equal between the samples. Another significant limitation of this technique arises when studying doped samples. Preparing specimens with specific surface facets often involves systematic thermal treatments which can lead to dopant redistribution within the sample. Any heterogeneities that arise can lead to a nonlinear relationship between the enthalpy of the drop solution and the surface area. Finally, it uses Hess's law engine to relate the measured enthalpy and surface energy by means of other reaction enthalpies which may not be known and which can compound the error [9, 24].

By comparison, water adsorption microcalorimetry requires only one specimen at room temperature. This specimen is nondestructively degassed to an anhydrous state and then exposed to water vapor, with the extent of adsorption measured using a water adsorption apparatus. At the same time, a microcalorimeter is utilized to quantify the energetic interactions between the water

and the surface of the powder. This method provides data indicating the average energy of the surfaces present in the studied specimen [9, 10]. The water adsorption experiment aims to measure the heat of water molecules' adsorption on the oxide's surface as a function of relative pressure. This is executed using a 3Flex dosimeter manufactured by Micromeritics attached to a DSC. The 3Flex doses water to the sample powder and records the relative pressures and the amount of adsorbed water. A Calvet-type microcalorimeter (Setaram Sensys Evo DSC) was used to measure the enthalpy of adsorption.

The sample powder was added to a test tube and degassed at elevated temperature under a vacuum to ensure the removal of all surface contaminants and water. Following the degassing, the sample was kept at a constant temperature, and water vapor was dosed in tiny amounts of 2 µmol to establish thermal equilibrium. The 3Flex controlled the water dosage and gave the sample chamber's relative pressure with respect to the empty reference tube. The DSC recorded the heat flow difference between the reference and the sample tube as a standard calorimetric experiment that gave the adsorption enthalpy.

The added water vapor was adsorbed on the surface of the powder creating a layer of water whose thickness increased with the dose. The two-interface model can describe this complex phenomenon of water adsorption. It can safely be assumed that at lower coverage, the system consists of a single-layer interface with water only attaching to the surface of the powder. Thus, we can use the Gibbs adsorption isotherm to relate the surface energy to the adsorbed water [27]. This is a chemisorption behavior where the water is adsorbed on the anhydrous surface by a dissociative behavior. As the number of doses increases, the water molecule experiences fewer

interactions with the surface while remaining highly polarized, making a physisorption layer. For high water coverage a thick layer of water exists, i.e., multi-layer adsorption, where the water molecules behave as a liquid-vapor interface. The Gibbs adsorption isotherm can also be used in this configuration to determine the surface energy of the powdered sample.

According to the process description, a comprehensive representation of the water adsorption process requires a Gibbs adsorption isotherm that accounts for two interfaces. The surface energy, γ (J/m^2), is measured from the adsorbed water equilibrium at the outermost layer with the water vapor or vacuum. We can derive the Gibbs adsorption isotherm for the two interfaces as:

$$SA \times d\gamma = -\sum_{I_1,I_2} \sum_i \theta_i d\mu_i \quad (6)$$

where μ is the chemical potential, θ is the adsorbed number of moles, *SA* is the surface area (m^2) measured using the BET theory explained above, the summation over i represents the excess constituents present at the interface, and I_1 and I_2 are the two types of interfaces.

We can average the chemical potential of all the constituents that are adsorbed at both the interfaces (averaging all chemisorbed and physisorbed water) and define a new variable μ_{ads}. Similarly, as the transition between the two interfaces of chemisorption and physisorption layers is not abrupt, the adsorbed water is expected to be combined with many adsorbed layers. Hence, we can replace the summation of adsorbed water molecules over different interfaces to be the total water molecules adsorbed, which is shown below:

$$\theta \approx \sum_{I_1,I_2} \sum_i \theta_i \quad (7)$$

We can then write equation 6 as:

$$SA \times d\gamma = -\theta d\mu_{ads} \quad (8)$$

Furthermore, the water added to the powder sample is not reacting with the bulk of the solid. Hence the only process occurring in the system is the adsorption reaction which is given as:

$$Surface + \theta_{ads}H_2O \rightleftharpoons Surface, \theta_{ads}H_2O_{(adsorbed)} \quad (9)$$

where θ_{ads} is the number of adsorbed water molecules. The microcalorimeter measures the heat of the reaction. Considering that the bulk energy remains constant with respect to the adsorption, we can neglect the entropic and the pV terms of the Gibbs free energy equation for the reversible reaction in equation 9 to arrive at an equality similar to equation 8:

$$SA \times d\gamma = -\theta dH_{ads} \quad (10)$$

where dH_{ads} is the measured heat of adsorption (J/mol). The relationship between two surface energies at different water coverage is established by equation 10. As discussed before, with increasing relative partial pressure, the water molecules behave as liquid and have a liquid-vapor interaction. At this point, the dH_{ads} will be the enthalpy of the water molecule adsorbing on liquid water, which is the saturation pressure. This value is the enthalpy of liquefaction of water and is known in the literature to be -44 kJ/mol at 25 ^{o}C [28]. At the same time, the surface energy of the system approaches the bulk liquid water value, which is 0.072 J/m^2 at 25 ^{o}C. These boundary conditions allow us to find a unique solution for every measured sample.

2.3 Results and Discussion

X-ray diffraction patterns of Y_2O_3 nanoparticles, nanosheets, and nanorods are shown in Figure 3. The pattern confirmed no contaminations in any of the three calcined nanostructures.

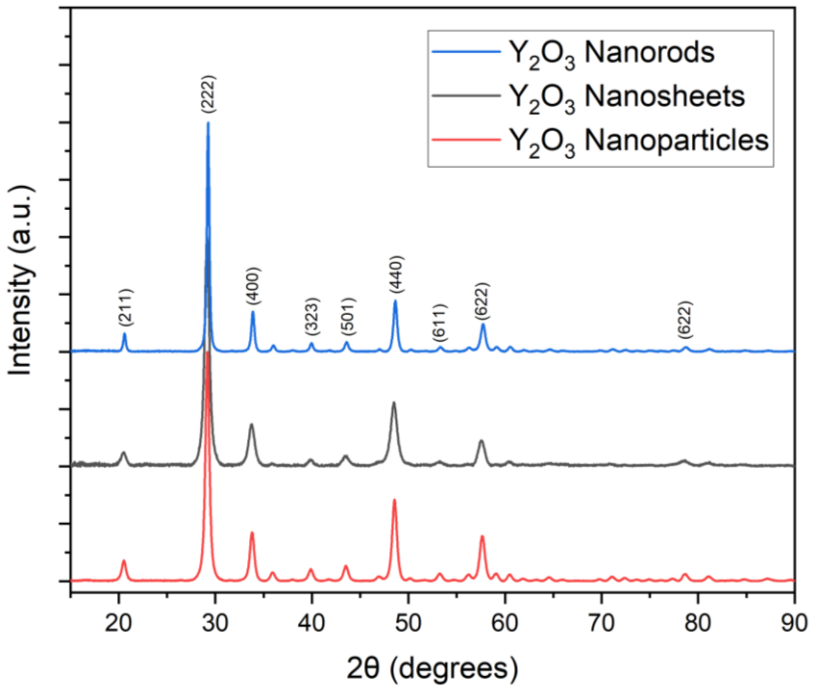

Figure 3: XRD spectra of calcined Y_2O_3 nanoparticles, nanorods, and nanosheets.

BET measurements were taken to determine the surface area of the nanostructures. The samples were first degassed at 250 ^oC under vacuum for 16 hours to remove all the surface contaminants before starting the BET run. A total of 3 runs were conducted on each sample to ensure the results were consistent and give a more statistically accurate measurement. The BET isotherm for yttrium oxide nanoparticles is shown in figure 4 and the calculated surface areas are reported in Table 1 below.

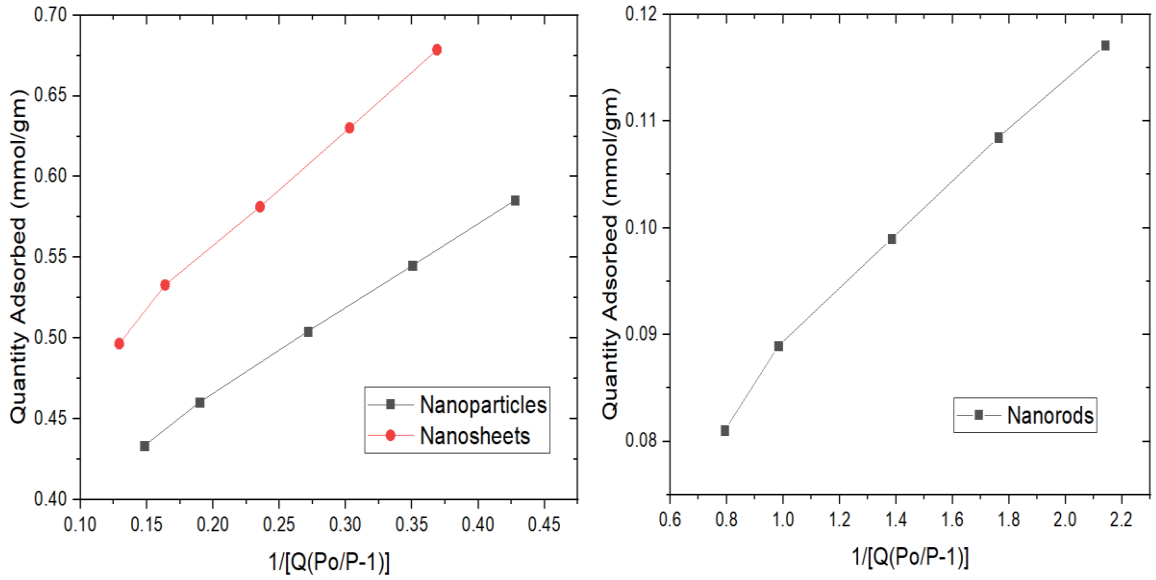

Figure 4: BET isotherms of nanoparticles, nanosheets, and nanorods.

Figure 5 shows the SEM images of Y_2O_3 nanosheets and nanorods. The images reveal the morphology of the nanostructures. Figures a) to d) show the nanosheets, and e) to h) show the nanorods. The SEM image used 10.0 kV beam voltage and a 3.0 spot size.

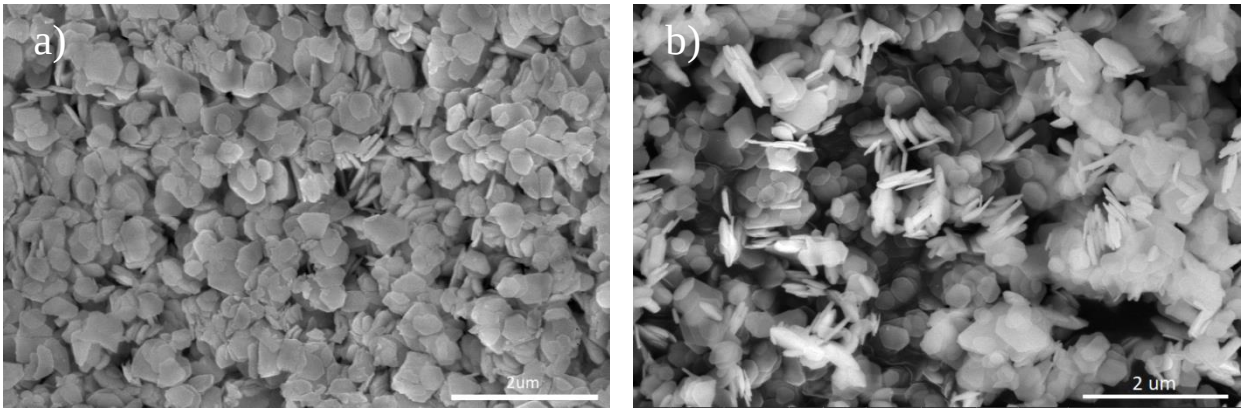

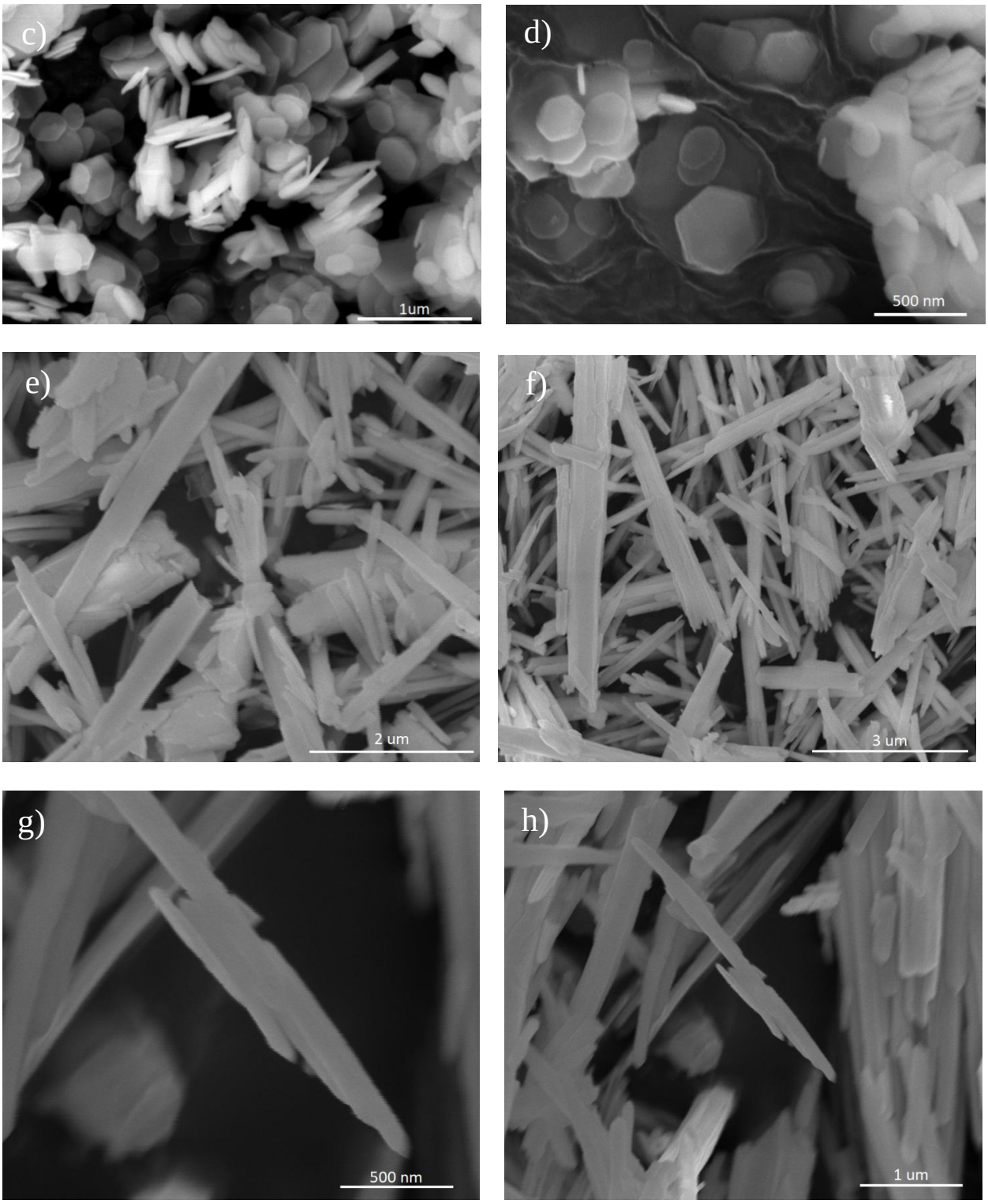

Figure 5: a-d) SEM images of Y_2O_3 nanosheets calcined at 600 ^oC. e-h) SEM images of Y_2O_3 nanorods calcined at 600 ^oC.

TEM microscopy was done on these nanostructures for a detailed analysis of morphology and orientation. Figure 6 shows the TEM images of nanosheets and nanorods.

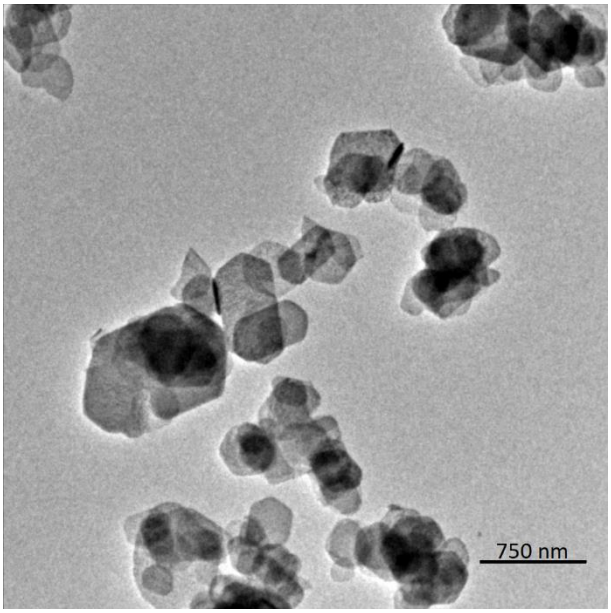

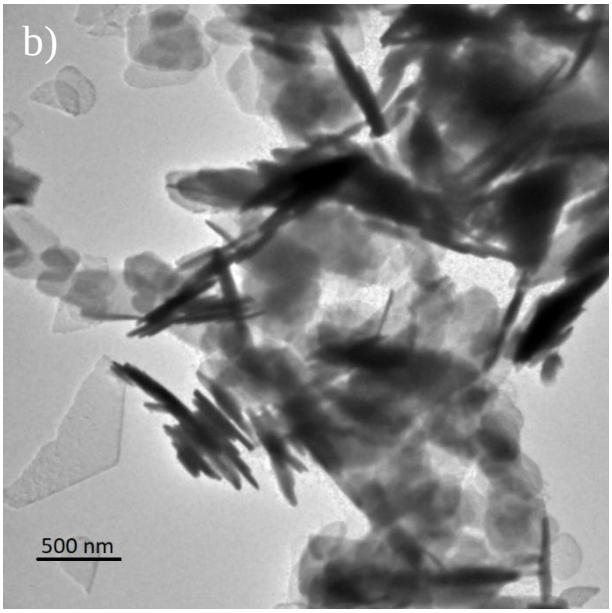

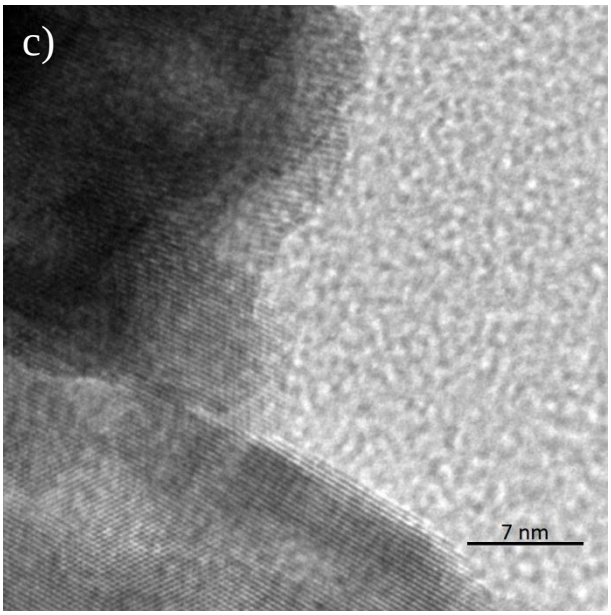

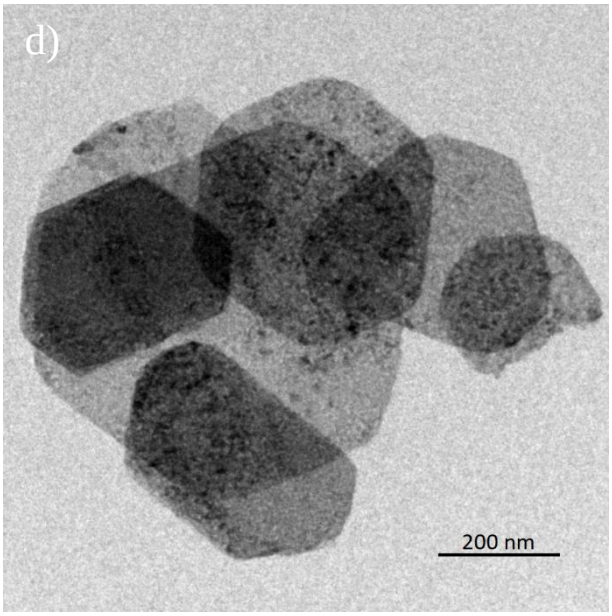

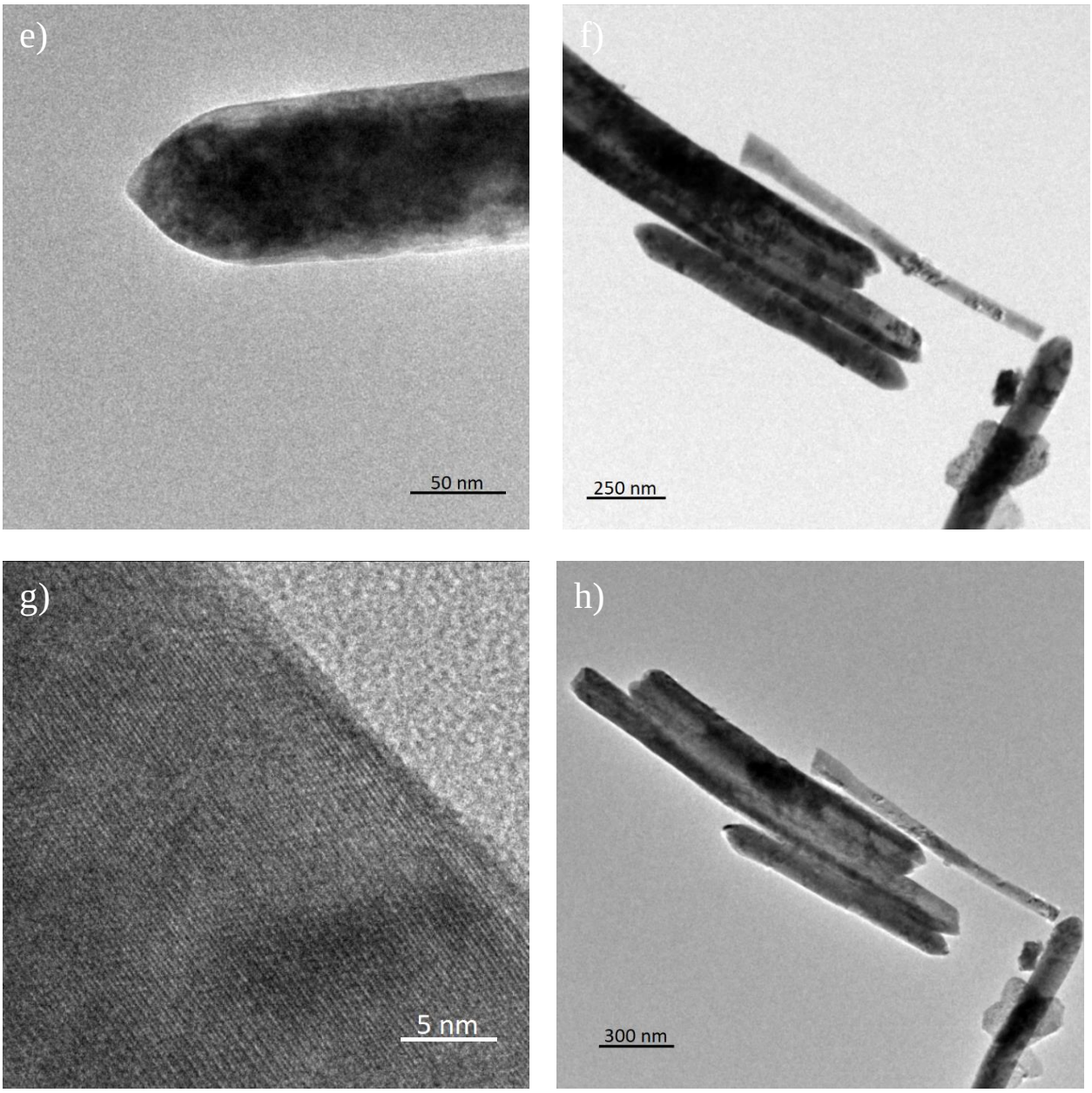

Figure 6: TEM images of Y_2O_3 a-d) nanosheets calcined at 600 ^oC and e-h) nanorods calcined at 600 ^oC.

Table 1 gives the crystallite sizes and the BET surface areas measured for the calcined powder samples. The crystallite size estimation of nanoparticles was done using the XRD pattern. The crystallite sizes of nanosheets and nanorods were estimated by analyzing the SEM and TEM

images. The BET surface area indicates that the surface area of the nanorods is much lower than that of the nanoparticles and nanosheets. This is due to the larger size of the nanorods along with agglomeration. The wide size distribution of the nanosheets and nanorods is reflected in the high uncertainties. Similarly, as the size of the nanoparticles is much less than that of the other two morphologies, the surface area being comparable to that of nanosheets is a result of nanoparticle agglomeration.

Table 1: Surface areas of nanoparticles, nanosheets, and nanorods.

	Nanoparticle	Nanosheet	Nanorod
Crystallite Size	17.1 ± 0.3 nm	313.6 ± 119.2 nm (Diameter) 32.8 ± 6.9 nm (Thickness)	80.9 ± 20.3 nm (Diameter) 1.3 ± 0.3 μm (Length)
Surface Area	46.46 ± 1.3 m^2/gm	55.56 ± 0.3 m^2/gm	9.75 ± 0.1 m^2/gm

Figure 7 shows the adsorption isotherms, water coverage as a function of relative pressure, and the differential heats of adsorption as a function of the relative pressure of water. The adsorption isotherm has the same relative shape as previous experiments in the literature [9, 10]. Prior to dosing the water, the sample was degassed under vacuum for 16 hours at 400 ^{o}C to ensure that the powder was free of all the surface contaminants along with water, hence making it an anhydrous surface.

During initial dosing the measured adsorption enthalpies are more negative than the condensation enthalpy of bulk water which is -44 kJ/mol, but it decreases in absolute magnitude to the bulk value at higher coverage and higher relative pressure.

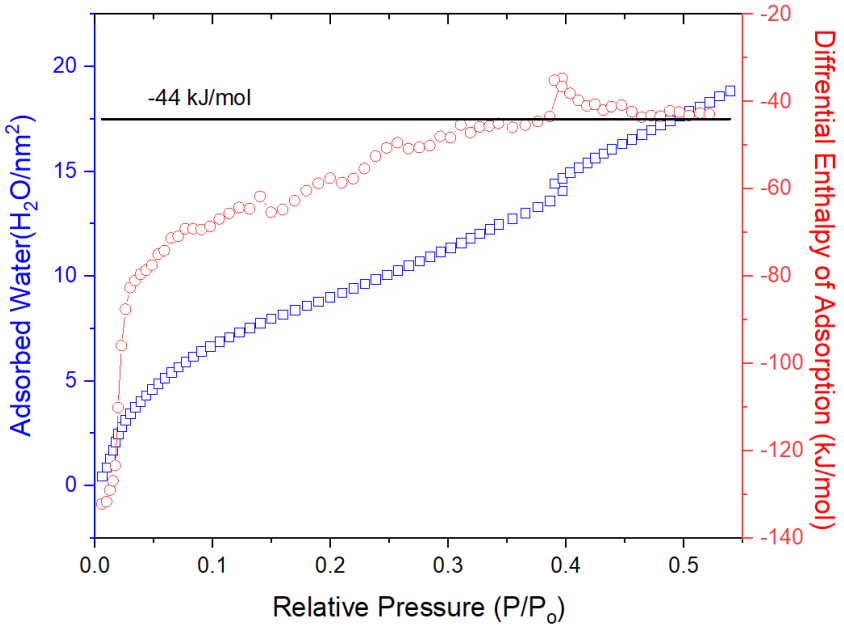

Figure 7: Water adsorption isotherm (blue square, left) of yttria nanoparticles. Differential heats of adsorption (red circle, right) as a function of relative pressure of the water adsorbed on the yttria nanoparticles. The plot converges to the enthalpy of water condensation (black line) at higher pressure.

The anhydrous surface energy curve as a function of water coverage for yttria nanoparticles is shown in figure 8. Yttria nanoparticles are anhydrous as before the water adsorption calorimetry run, the sample was degassed at higher temperature to ensure that there is no water content or any contamination on the surface. The average surface energy for Y_2O_3 nanoparticles is measured to be 1.60 J/m^2. The experimental surface energy results compare well with the literature data as shown in table 2. However, due to instrument failure and other limitations the surface energy calculations of the nanostructures were not possible in the time frame.

Table 2: Surface energy(J/m^2) measured using water adsorption calorimetry compared to literature.

	This work	Technique used
Y_2O_3	1.60	Water adsorption microcalorimetry (This work)
	1.66 [27]	High temperature oxide-melt calorimetry
	1.42 [5]	Heats of sintering
	2.16 [22]	High Temperature contact angle

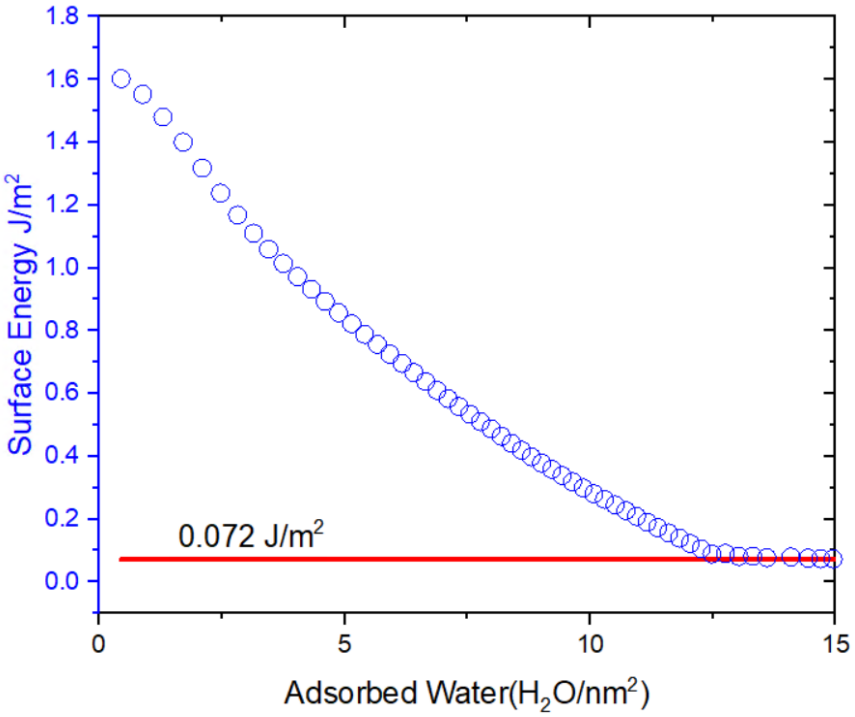

Figure 8: Surface energy (J/m^2) determined from water adsorption experiments as a function of water coverage.

Chapter 3: Atomistic Simulations of Surface Energies of Y_2O_3

3.1 Introduction

Structural characteristics drive polycrystalline engineering materials and their properties at the atomic scale; hence, it is important to study the free surfaces and interfaces. For example, in ceramic oxides, nanoparticles' catalytic properties and stability depend on the type and structure of exposed free surfaces. Analyzing the atomic structure of these interfaces involves examining the underlying crystallographic symmetries [30].

Alumina and yttria are ubiquitous in the class of refractory ceramics. However, compared to alumina, the study of yttria's structure and free surfaces has been negligible. Studies have shown the surface energy trends of γ-Al_2O_3 and how the different terminating surfaces and structure symmetry affect the surface energy. On the other hand, only a few experimental measurements have been conducted for yttria, and there is a complete lack of theoretical support and relevant data. Despite this lack of data, γ-Al_2O_3 can be used as a reference material to study and predict the trends in Y_2O_3 since both have a similar cubic structure with a space group of $Ia\bar{3}$. However, γ-Al_2O_3 also studied as a defective spinel with a C2/m space group. [31, 32].

Atomistic simulations using molecular dynamics can serve as a predictive tool to allow the calculation of surface energies of low-index surfaces. These simulations can help to understand the trends of energy with respect to surface orientation, as well as validate the experimental observations. They also give us the opportunity to explore a wide range of conditions that might not be experimentally feasible.

3.2 Methods and Setup

Atomistic simulations were done using molecular dynamics and were carried out using the Large-scale Atomic/Molecular Massively Parallel Simulator (LAMMPS) [33, 34]. The fundamental principle underlying molecular dynamics is the application of classical mechanics to atomistic systems. The forces acting on all the atoms are calculated, and Newton's equations are solved to determine the motions of the atoms in response to those forces [35]. Interatomic potential functions, including short-range repulsive and long-range attractive interactions, determine the atoms' interactions. Additionally, since the system we are working with is a ceramic (an ionic solid with charged species), it is necessary to include electrostatic or coulombic interactions between the ions.

Periodic boundary conditions (PBC) are usually applied in molecular dynamics simulations to maintain the structure and conserve the system's mass. If a particle leaves a computational cell from one side, then an equivalent particle enters the opposite side of the cell [35]. The NPT ensemble was used to conduct the simulations where the number of particles (N), the pressure (P), and the temperature (T) of the system were held constant at each time step. The positions and velocities of the particles were updated after each time step, and the positions and velocities were calculated again. The simulation results depend on various parameters such as the initial arrangement or structure of atoms, the number of time steps, the size of the time step, the number of atoms, the cutoff radius of the potential, and the energy minimization algorithm.

The crystal structure data for Y_2O_3 was retrieved from the Materials Project (mp-2652) from database version v2022.10.28 [36]. Yttrium oxide (Y_2O_3) exhibits a structure similar to

corundum and crystallizes in the cubic $Ia\bar{3}$ space group, as shown in Figure 9, with two distinct Y^{3+} sites. At the first Y^{3+} site, Y^{3+} ions are connected to six equivalent O^{2-} ions, forming distorted YO_6 octahedra that share edges and corners. The octahedra at the corners exhibit tilt angles ranging from 54 to 56 degrees and have Y–O bond distances between 2.25 and 2.33 Å. At the second Y^{3+} site, Y^{3+} ions are bonded to six equivalent O^{2-} ions, forming a mixture of YO_6 octahedra that share edges and corners but without significant distortion. The tilt angle of the corner-sharing octahedra is 56 degrees, and all Y–O bond lengths measure 2.28 Å. O^{2-} ions are bonded to four Y^{3+} atoms, resulting in a mixture of distorted OY_4 trigonal pyramids that share edges and corners [36].

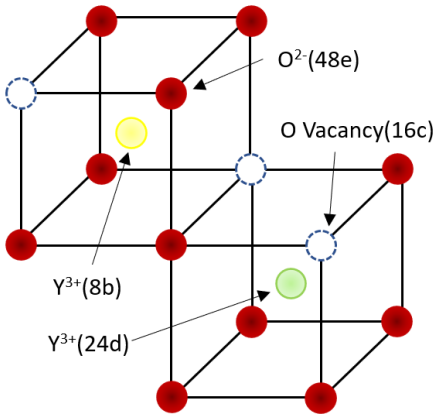

Figure 9: Structure of cubic Y2O3.

3.2.1 Verification of various interactions models:

There are various interaction potentials for yttrium oxide available in the literature for us to use [37-43]. However, as each study focused on different ceramic properties, we performed a series of MD simulations to evaluate which model would yield the best results for our research. Since we are interested in the thermodynamic properties of yttria, we assessed how well each model

predicted the melting temperature of Y_2O_3 by a simple technique where we evaluated the potential energy as the simulation cell was heated to 7000 K. The simulation cell consisted of a 3x3x3 unit cell of Y_2O_3, with each unit cell composed of 80 atoms for a total of 2160 atoms. Periodic boundary conditions in each direction made the simulation resemble a bulk crystal. Constant pressure simulations were performed for 750,000 steps with a time step of 1 ns, and the temperature was updated after 3000-time step increments. The cutoff radius for the potential was 8 Å. The calculated energies as a function of temperature are shown in figure 10, with the sudden jump in potential energy indicating the melting temperature [44]. The interaction potentials used in this study are given in the table 3. We found that the model provided by Du et al. [38] was the closest approximation of the experimental melting temperature, which was determined by XRD of levitated liquid yttrium oxide as being 2706±5 K [45].

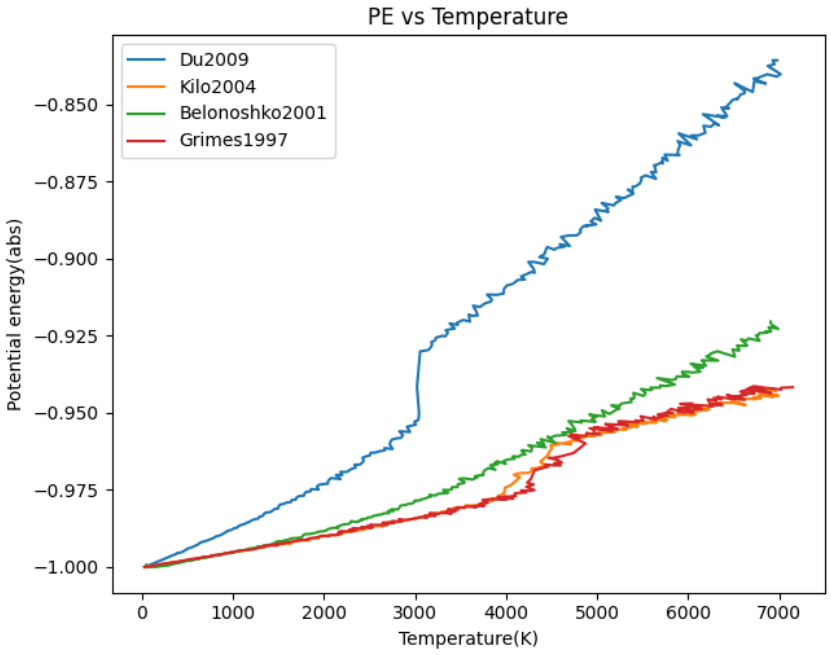

Figure 10: Potential Energy as a function of temperature for different interatomic potentials

Table 3: Interatomic potentials from literature used in the study

Pair	A(eV)	ρ(Å)	C(eV. Å^{-6})	Reference
$O^{-1.2}$ - $O^{-1.2}$	1844.7458	0.343645	192.58	38
$Y^{1.8}$ - $O^{-1.2}$	29526.977	0.211377	50.477	
$Y^{1.8}$ - $Y^{1.8}$	0.0	-	0.0	
$O^{-1.2}$ - $O^{-1.2}$	4672.5590	0.187987	0.0	41
$Y^{1.8}$ - $O^{-1.2}$	1486.4180	0.172628	0.0	
$Y^{1.8}$ - $Y^{1.8}$	2480.6927	0.232298	0.0	
O^{-2} - O^{-2}	22764.3	0.149	27.89	42
Y^{3} - O^{-2}	1325.6	0.3461	0.0	
Y^{3} - Y^{3}	0.0	-	0.0	
O^{-2} - O^{-2}	9547.96	0.21916	32.0	43
Y^{3} - O^{-2}	1766.40	0.33849	19.43	
Y^{3} - Y^{3}	0.0	-	0.0	

Hence, we have used the Buckingham potential form for the long and short-range interactions and a Coulombic contribution given by Du et al. [38] as

$$U_{ij}(r_{ij}) = \frac{1}{4\pi\varepsilon_o}\frac{Z_i Z_j e^2}{r_{ij}} + A\exp\left(\frac{-r_{ij}}{\rho}\right) - \frac{C}{r_{ij}^6} \quad (11)$$

where $U_{ij}(r_{ij})$ is the potential, ε_o is the dielectric constant of vacuum and r_{ij} is the distance between the atoms i and j. Z_i and Z_j are the effective charges in units of the fundamental charge. The parameters and effective charges used for this work are given in the following table. The cutoff radius was kept at 8 Angstroms.

3.2 Results

Table 4: Potential Parameters Used in MD Simulations

Pair	A (kJ/mol)	ρ (Å)	C (kJ/(mol. $Å^6$)
$O^{-1.2}$ - $O^{-1.2}$	178069.65	0.343645	18589.364
$Y^{1.8}$ - $O^{-1.2}$	2850180.41	0.211377	4872.445
$Y^{1.8}$ - $Y^{1.8}$	0.0	-	0.0

Having finalized the potential model, the next step was to study the surfaces and calculate the surface energies. Various studies have investigated the energies of different surfaces of γ-alumina using density functional theory and molecular dynamics [46-48]. They have shown that the surface energies vary drastically with surface orientation and can also depend on the terminating layers for these orientations. We have examined the (100), (110), (111), and (121) planes, these likely being the most relevant in practice based on the studies on γ-alumina. Viewed along the corresponding normal directions, each lattice structure contains two mirror planes for which local charge neutrality is relatively straightforward to enforce. Using these mirror planes as different terminating surfaces gives *a* and *b* variants for each surface orientation. These terminating surfaces are shown in figure 11. These surfaces of different orientations were constructed using Atomsk, an open-source command-line program for creating, manipulating,

and converting data files for atomic-scale simulations [49]. The bulk structure was built with 10x10x10 unit cells for a total of 80,000 atoms. Periodic boundary conditions were applied in all three directions to simulate a bulk crystal. A surface was created by adding an empty simulation box with a height equal to half the slab thickness above the slab. After creating structures with surfaces in the desired orientations, atomic layers were deleted using Ovito until the desired terminating layer was on the surface [50]. Ovito was also used as the visualization tool for the structure data files. Charge neutrality was maintained during the deletion of atoms.

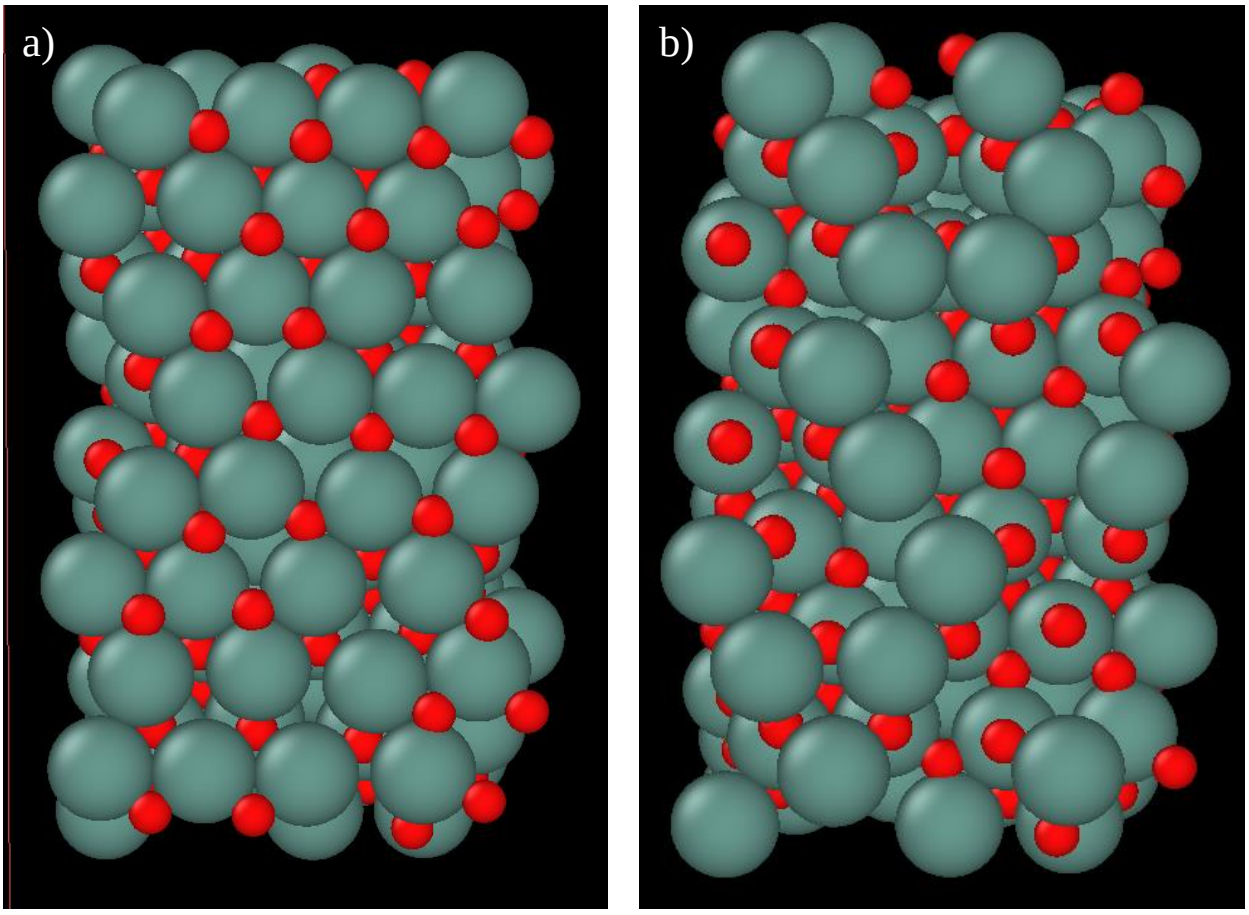

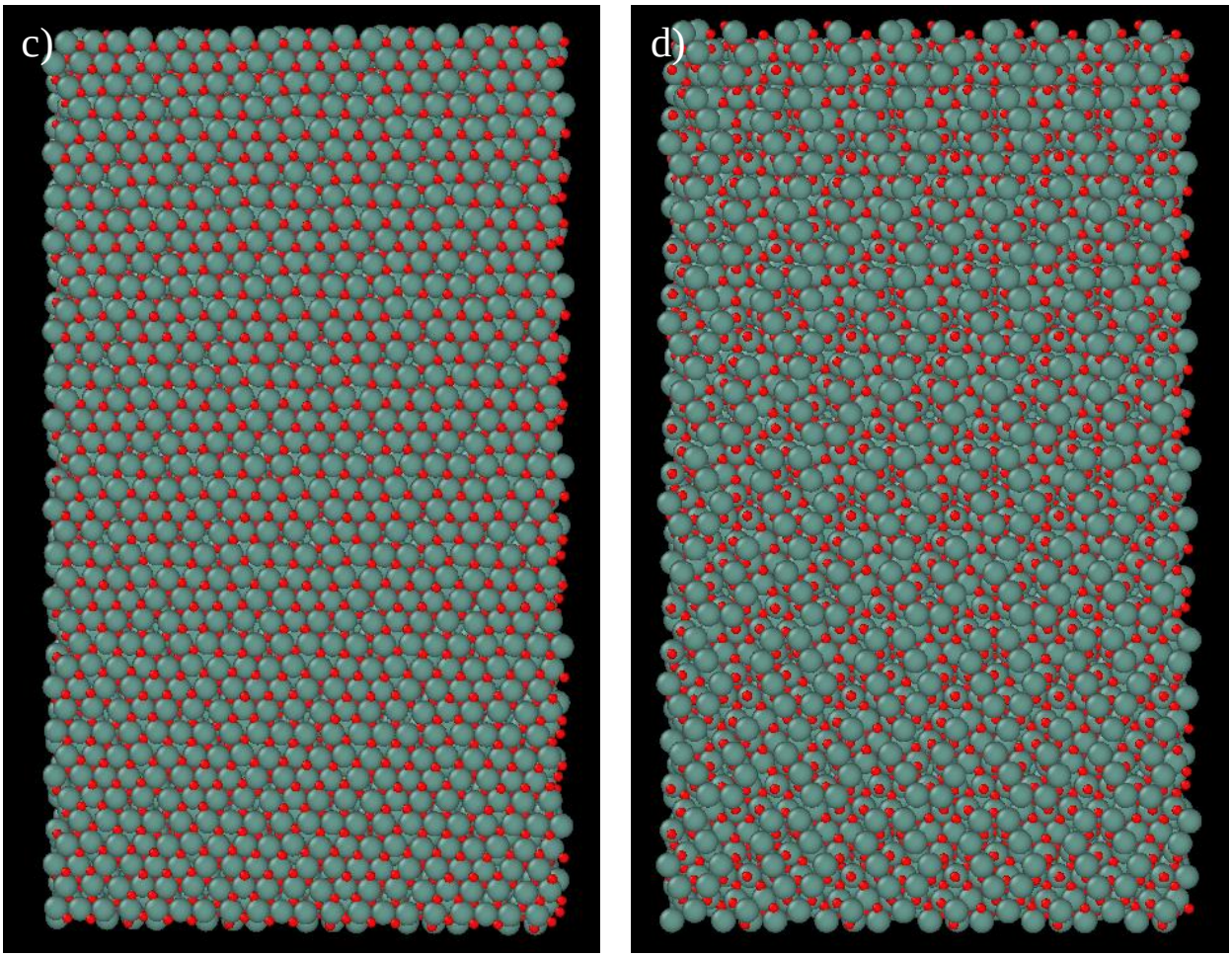

Figure 11: a) Terminating surface of 111a plane (1 unit cell), b) Terminating surface of 111b plane (1 unit cell), c) Terminating slab surface of 111a plane, d) Terminating slab surface of 111b plane.

Once these stable structures were obtained, MD simulations were performed using LAMMPS. The simulations were run for 1,318,000-time steps with a time step of 1 ns, with the initial 1,000,000 steps being used for temperature equilibration at 2332 K, which is 0.7 of the simulated melting point. After homogenization, the structure was slowly quenched to 0 K to achieve a low-energy reference configuration by decrementing the temperature by 22 K every 3000 time steps. Figure 12 shows the simulation cell at each interval. Initially, the cell is ordered, and as it is

heated, the disordering increases. The quenching allows surface reconstruction, which is shown in Figure c.

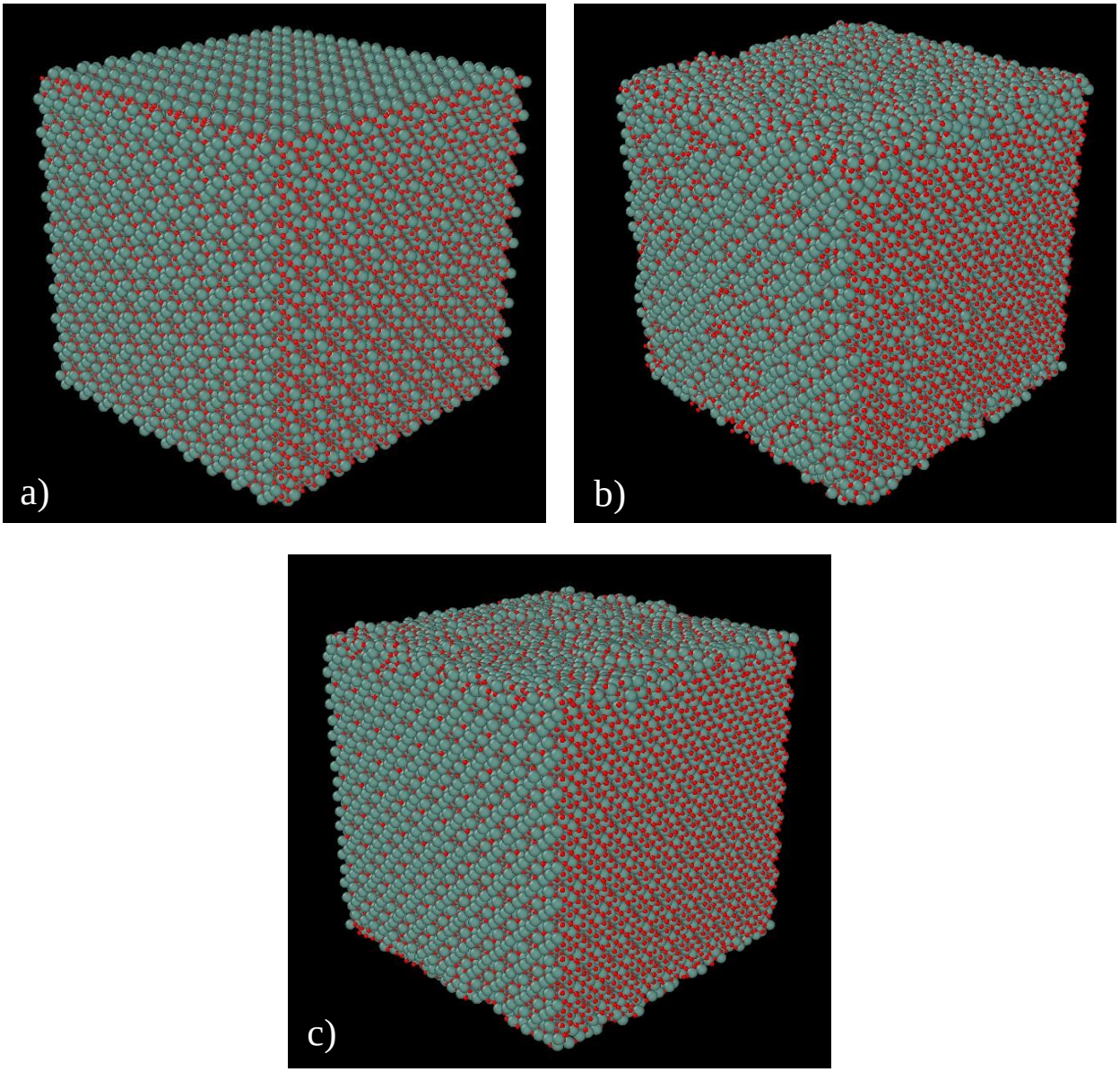

Figure 12: Simulation cell for the 100a slab, with a free surface in the z-direction. a) Before heating, b) after heating, and c) after a slow quench with a reconstructed surface.

The surface energies were calculated from the potential energy per atom and the area of the surface by the following equation:

$$\gamma = \frac{(E_{surface} - E_{bulk}) * N}{2 * (Area\ of\ the\ slab)} \quad (12)$$

where γ is the surface energy of the structure, E is the potential energy per atom of either the structure with the surface or the bulk, N is the number of atoms in the simulation cell, and A is the area of the slab's surface.

Table 5 shows the calculated surface energy values of these different terminating planes of different orientations, along with the area of the surface slab and the number of atoms present in the simulation cell. The energy per atom of the bulk (E_{bulk}) was calculated to be -1.7566×10^{-18} J/atom.

Table 5: Computed Surface Energies of Y_2O_3 crystal orientations

Surface	Energy per atom of surface ($E_{surface}$)(10^{-18} J/atom)	Area (nm^2)	Atoms	Surface Energy (J/m^2)
100a	-1.7506	11225.97	80000	2.12
100b	-1.7510	11215.49	84000	2.08
110a	-1.7524	11924.17	102000	1.79
110b	-1.7525	11919.50	105000	1.79
111a	-1.7545	9737.58	120000	1.23
111b	-1.7542	9727.87	130000	1.60
121a	-1.7539	6883.41	92000	1.78

121b	-1.7537	6881.01	94000	1.94

It can be seen in the table that the surface energy varies significantly as we change the crystal orientations. This is because of the atomic spacing and number of atoms in that particular plane direction. The difference in the number of atoms for each surface is due to deleting the atoms to create these surfaces. Furthermore, the slabs' thickness was kept to at least 8 unit cells to minimize the interactions between the surfaces.

Chapter 4: Correlation and Prediction of Surface Energies of Y_2O_3

4.1 Discussion

The surface energy of nanoparticles was measured experimentally through water adsorption calorimetry. This technique's experimental limitation is that the energy of all exposed surfaces is measured at once, complicating the process of inferring energies of specific surfaces. However, we can correlate the atomistic simulation and the calculated surface energies with the experimental results to predict the surface energies of different nanostructures.

Considering the case of a generic faceted nanoparticle, it is reasonable to assume that the most significant contributions to the surface area will be facets with the lowest Miller indices. We therefore assume that, to within an error comparable to that for the measurement of the nanoparticle geometry, the average surface area and average surface energy available through experimental measurements are related to the energies of specific surfaces as follows:

$$\gamma_{avg} \times A_{avg} = \gamma_{111} \times A_{111} + \gamma_{110} \times A_{110} + \gamma_{100} \times A_{100} \quad (13)$$

where the γ is the surface energy, A is the respective surface area, the subscript represents the exposed plane orientation, and the average is the surface energy and surface area as measured using microcalorimetry and BET. While not a conclusive validation, it is gratifying that the experimental average surface energy of Y_2O_3 nanoparticles reported in Table 2 and the simulated surface energies of specific planes reported in Table 5 are consistent with a feasible set of facet areas in equation 13.

While the experimental values for the surface energies of the nanosheets and nanorods are not yet available, we can use equation 13 to predict what they should be within a reasonable error. The size distribution of the nanosheets and nanorods is given in Table 1. Additionally, Y_2O_3 is a cubic crystal, and the electron microscopy images of nanosheets show a six-fold symmetry of these sheets around the surface normal direction. This indicates that the surface plane is likely {111} type, implying that the perpendicular facets should be of {110} type; this is consistent with these facets being at relative angles of 120°. Specializing equation 13 and dividing through by the average area gives the following:

$$A_{111} \times \gamma_{111} + A_{110} \times \gamma_{110} = \gamma_{NS} \quad (14)$$

where A is the ratio of the area of a specific plane to the total surface area and γ_{NS} is the average surface energy of the nanosheet.

We can deduce a similar equation for the nanorods. Electron microscopy image analysis of the nanorods suggests that the plane along the axis of the rod has a six-fold symmetry identical to the nanosheets. By the same reasoning as before, the plane perpendicular to the axis of the nanorods is likely of {111} type, and that perpendicular to the rod diameter is likely of {110} type. This means that equation 14 can also be used to obtain the surface energy of these nanorods.

Table 6 shows the expected average surface energies of the nanostructures given by inserting the MD predictions in Table 5 and the area ratios in Table 1 into equation 14.

Table 6: Estimated surface energies of nanostructures

	$Area_{111}$	γ_{111} J/m^2	$Area_{111}$	γ_{110} J/m^2	γ J/m^2

Nanosheets	0.67	1.23	0.33	1.79	1.41
Nanorods	0.02		0.98		1.78

The surface energies of {110} type and {111} type were taken to be the minimum of the two terminating surfaces, these being the most likely from a statistical standpoint. The surface energy of nanorods is higher than that of the nanosheets because the nanorods have a negligible surface area of the lower energy {111} type plane, whereas it is significant for the nanosheets.

Furthermore, we can use the same equation 14 to develop a system of equations to solve for the experimental {111} and {110} surface energies when the water absorption experiments become available. The two versions of equation 14 for the nanosheets and the nanorods can collectively be written as:

$$\begin{bmatrix} A_{111,NS} & A_{110,NS} \\ A_{111,NR} & A_{110,NR} \end{bmatrix} \begin{bmatrix} \gamma_{111} \\ \gamma_{110} \end{bmatrix} = \begin{bmatrix} \gamma_{NS} \\ \gamma_{NR} \end{bmatrix} \quad (15)$$

We can solve this system as

$$\begin{bmatrix} \gamma_{111} \\ \gamma_{110} \end{bmatrix} = A^{-1} \begin{bmatrix} \gamma_{NS} \\ \gamma_{NR} \end{bmatrix}, \quad (16)$$

where A^{-1} is the inverse of the area matrix and find γ_{111} and γ_{110} as soon as the experiments are complete.

Chapter 5: Conclusion and Future Works

5.1 Conclusion

This dissertation gives a detailed analysis of the surface energies of specific crystallographic planes of Y_2O_3. It was observed that the surface energies depend not only on the orientation of the planes but on the terminating surfaces as well. The methods used to synthesize nanosheets and nanorods were formulated in a detailed manner for reproducibility. Several characterization techniques (XRD, BET, SEM, TEM, and water adsorption microcalorimetry) were used to study the structure, morphology, and surface energy of Y_2O_3 nanostructures experimentally. Molecular dynamics simulations were carried out to estimate the surface energies of various planes directly, and to eventually corroborate the surface energy values inferred from experimental results.

5.2 Future Work

The experiments to measure the surface energies of nanosheets and nanorods are yet to be conducted. Synthesis methods can be refined for the nanosheets and nanorods to synthesize smaller nanostructures with a more uniform size distribution. Characterization using electron microscopy and analysis of electron diffraction patterns would help to understand the crystal orientation of various surface facets. Adding dopants during the synthesis of Y_2O_3 nanostructures synthesis and studying of the segregation behavior of the dopants would be critical to control the surface energies of the specific crystal orientations. Molecular dynamics simulations could assist in predicting if the segregation is surface-orientation dependent or is homogeneous throughout the structure. This would require a more complex model that evaluates the segregation behavior of dopants as a function of both valency and concentration though. Furthermore, the

nanostructures can be sintered using the spark plasma sintering technique to generate layered pallets. The morphological anisotropy in the initial powder would give rise to different diffusion pathways and different thermodynamic driving forces than for conventional powders. Hence, it would induce structural anisotropy and mechanical anisotropy in the final pallets.

Reference

[1] Tam, J., Feng, B., Ikuhara, Y., Ohta, H., & Erb, U. (2018). Crystallographic orientation–surface energy–wetting property relationships of rare earth oxides. *Journal of Materials Chemistry A*, *6*(38), 18384-18388.

[2] Castro, R., & Van Benthem, K. (Eds.). (2012). *Sintering: mechanisms of convention nanodensification and field assisted processes* (Vol. 35). Springer Science & Business Media.

[3] Kang, S. J. L. (2004). *Sintering: densification, grain growth and microstructure*. Elsevier.

[4] Castro, R. H. R. (2019). Controlling sintering and grain growth of nanoceramics. *Cerâmica*, *65*, 122-129.

[5] Nakajima, K., & Castro, R. H. (2020). Thermodynamics and kinetics of sintering of Y2O3. *Journal of the American Ceramic Society*, *103*(9), 4903-4912.

[6] Xu, Y. N., Gu, Z. Q., & Ching, W. Y. (1997). Electronic, structural, and optical properties of crystalline yttria. *Physical Review B*, *56*(23), 14993.

[7] Curtis, C. E. (1957). Properties of yttrium oxide ceramics. *Journal of the American Ceramic Society*, *40*(8), 274-278

[8] Rajakumar, G., Mao, L., Bao, T., Wen, W., Wang, S., Gomathi, T., ... & Zhang, X. (2021). Yttrium oxide nanoparticle synthesis: an overview of methods of preparation and biomedical applications. *Applied Sciences*, *11*(5), 2172.

[9] Castro, R. H., & Quach, D. V. (2012). Analysis of anhydrous and hydrated surface energies of gamma-Al2O3 by water adsorption microcalorimetry. *The Journal of Physical Chemistry C*, *116*(46), 24726-24733.

[10] Drazin, J. W., & Castro, R. H. (2014). Water adsorption microcalorimetry model: deciphering surface energies and water chemical potentials of nanocrystalline oxides. *The Journal of Physical Chemistry C*, *118*(19), 10131-10142.

[11] Kellett, B. J., & Lange, F. F. (1989). Thermodynamics of densification: I, sintering of simple particle arrays, equilibrium configurations, pore stability, and shrinkage. *Journal of the American Ceramic Society*, *72*(5), 725-734.

[12] Lange, F. F., & Kellett*, B. J. (1989). Thermodynamics of densification: II, grain growth in porous compacts and relation to densification. *Journal of the American Ceramic Society*, *72*(5), 735-741.

[13] Slamovich, E. B., & Lange, F. F. (1993). Densification of large pores: II, driving potentials and kinetics. *Journal of the American Ceramic Society*, *76*(6), 1584-1590.

[14] Lange, F. F. (2008). Densification of powder compacts: An unfinished story. Journal of the European Ceramic Society, 28(7), 1509-1516.

[15] Wakai, F., Yoshida, M., & Kashyap, B. P. (2006). Influence of particle arrangement on coarsening during sintering of three spherical particles. *Journal of the Ceramic Society of Japan*, *114*(1335), 974-978.

[16] Searcy, A. W. (1985). Driving force for sintering of particles with anisotropic surface energies. *Journal of the American Ceramic Society*, *68*(10), C-267.

[17] Matsunaga, T., Takeshita, S., & Isobe, T. (2015). Synthesis, photoluminescence, and photostability of Y2O3: Bi3+, Eu3+ nanosheets. *Journal of Luminescence*, *165*, 62-67.

[18] Priya, R., Kainth, S., Kumar, D., Sharma, P., Diwan, P. K., & Pandey, O. P. (2022). Investigating transformation kinetics of yttrium hydroxide to yttrium oxide. *Materials Chemistry and Physics*, *287*, 126243.

[19] Brunauer, S., Emmett, P. H., & Teller, E. (1938). Adsorption of gases in multimolecular layers. *Journal of the American chemical society*, *60*(2), 309-319.

[20] Ambroz, F., Macdonald, T. J., Martis, V., & Parkin, I. P. (2018). Evaluation of the BET Theory for the Characterization of Meso and Microporous MOFs. *Small methods*, *2*(11), 1800173.

[21] Hwang, N., & Barron, A. R. (2011). BET surface area analysis of nanoparticles. *The connexions project*, 1-11.

[22] Triantafyllou, G., Angelopoulos, G. N., & Nikolopoulos, P. (2010). Surface and grain-boundary energies as well as surface mass transport in polycrystalline yttrium oxide. *Journal of materials science*, *45*, 2015-2022.

[23] Kendall, K., McN. Alford, N., & Birchall, J. D. (1987). A new method for measuring the surface energy of solids. *Nature*, *325*(6107), 794-796.

[24] McHale, J. M., Auroux, A., Perrotta, A. J., & Navrotsky, A. (1997). Surface energies and thermodynamic phase stability in nanocrystalline aluminas. *Science*, *277*(5327), 788-791.

[25] Ushakov, S. V., & Navrotsky, A. (2005). Direct measurements of water adsorption enthalpy on hafnia and zirconia. *Applied Physics Letters*, *87*(16).

[26] Zhang, P., Xu, F., Navrotsky, A., Lee, J. S., Kim, S., & Liu, J. (2007). Surface enthalpies of nanophase ZnO with different morphologies. *Chemistry of Materials*, *19*(23), 5687-5693.

[27] Adamson, A. W. (1968). An adsorption model for contact angle and spreading. *Journal of Colloid and Interface Science*, *27*(2), 180-187.

[28] Bolis, V., Fubini, B., Marchese, L., Martra, G., & Costa, D. (1991). Hydrophilic and hydrophobic sites on dehydrated crystalline and amorphous silicas. *Journal of the Chemical Society, Faraday Transactions*, *87*(3), 497-505.

[29] Zhang, P., Navrotsky, A., Guo, B., Kennedy, I., Clark, A. N., Lesher, C., & Liu, Q. (2008). Energetics of cubic and monoclinic yttrium oxide polymorphs: phase transitions, surface enthalpies, and stability at the nanoscale. *The Journal of Physical Chemistry C*, *112*(4), 932-938.

[30] Frolov, T., & Mishin, Y. (2009). Temperature dependence of the surface free energy and surface stress: An atomistic calculation for Cu (110). *Physical review B*, *79*(4), 045430.

[31] Prins, R. (2020). On the structure of γ-Al2O3. *Journal of Catalysis*, *392*, 336-346.

[32] Sun, J., Stirner, T., & Matthews, A. (2006). Structure and surface energy of low-index surfaces of stoichiometric α-Al2O3 and α-Cr2O3. *Surface and Coatings Technology*, *201*(7), 4205-4208.

[33] Plimpton, S. (1995). Fast parallel algorithms for short-range molecular dynamics. *Journal of computational physics*, *117*(1), 1-19.

[34] Thompson, A. P., Aktulga, H. M., Berger, R., Bolintineanu, D. S., Brown, W. M., Crozier, P. S., ... & Plimpton, S. J. (2022). LAMMPS-a flexible simulation tool for particle-based materials modeling at the atomic, meso, and continuum scales. *Computer Physics Communications*, *271*, 108171.

[35] LeSar, R. (2013). *Introduction to computational materials science: fundamentals to applications*. Cambridge University Press.

[36] The Materials Project. *Materials Data on Y2O3 by Materials Project*. United States.

[37] Liu, C., Zhang, Y., & Li, S. (2021). Yttrium Oxide (Y2O3) Nanoparticle Crystallization in Gas-Phase Synthesis: A Molecular Dynamics Study. *Energy & Fuels*, *35*(6), 5281-5290.

[38] Du, J. (2009). Molecular dynamics simulations of the structure and properties of low silica yttrium aluminosilicate glasses. *Journal of the American Ceramic Society*, *92*(1), 87-95.

[39] Uritsky, M. Z., & Tsidilkovski, V. I. (2012). Proton transport in doped yttrium oxide. Monte-Carlo simulation. *Russian Journal of Electrochemistry*, *48*, 917-921.

[40] Alvarez, L. J., San Miguel, M. A., & Odriozola, J. A. (1999). Effects of nonstoichiometry in the melting process of Y 2 O 3 from molecular dynamics simulations. *Physical Review B*, *59*(17), 11303.

[41] Belonoshko, A. B., Gutierrez, G., Ahuja, R., & Johansson, B. (2001). Molecular dynamics simulation of the structure of yttria Y 2 O 3 phases using pairwise interactions. *Physical Review B*, *64*(18), 184103.

[42] Kilo, M., Taylor, M. A., Argirusis, C., Borchardt, G., Jackson, R. A., Schulz, O., ... & Weller, M. (2004). Modeling of cation diffusion in oxygen ion conductors using molecular dynamics. *Solid State Ionics*, *175*(1-4), 823-827.

[43] Grimes, R. W., Busker, G., McCoy, M. A., Chroneos, A., Kilner, J. A., & Chen, S. P. (1997). The effect of ion size on solution mechanism and defect cluster geometry. *Berichte der Bunsengesellschaft für physikalische Chemie*, *101*(9), 1204-1210.

[44] Ahuja, R., Belonoshko, A. B., & Johansson, B. (1998). Melting and liquid structure of aluminum oxide using a molecular-dynamics simulation. *Physical Review E*, *57*(2), 1673.

[45] Krishnan, S., Ansell, S., & Price, D. L. (1998). X-ray Diffraction from Levitated Liquid Yttrium Oxide. *Journal of the American Ceramic Society*, *81*(7), 1967-1969.

[46] Pinto, H. P., Nieminen, R. M., & Elliott, S. D. (2004). Ab initio study of γ− Al 2 O 3 surfaces. *Physical review B*, *70*(12), 125402.

[47] Digne, M., Sautet, P., Raybaud, P., Euzen, P., & Toulhoat, H. (2004). Use of DFT to achieve a rational understanding of acid–basic properties of γ-alumina surfaces. *Journal of Catalysis*, *226*(1), 54-68.

[48] Blonski, S., & Garofalini, S. H. (1993). Molecular dynamics simulations of α-alumina and γ-alumina surfaces. *Surface Science*, *295*(1-2), 263-274.

[49] Hirel, P. (2015). Atomsk: A tool for manipulating and converting atomic data files. *Computer Physics Communications*, *197*, 212-219.

[50] Stukowski, A. (2009). Visualization and analysis of atomistic simulation data with OVITO–the Open Visualization Tool. *Modelling and simulation in materials science and engineering*, *18*(1), 015012.